Self-stabilization mechanism in ultra-stable Fourier domain mode-locked (FDML) lasers

MARK SCHMIDT,[1,*] (iD) **TOM PFEIFFER,**[2] (iD) **CHRISTIN GRILL,**[2] **ROBERT HUBER,**[2] (iD) **AND CHRISTIAN JIRAUSCHEK**[1] (iD)

[1]*TUM Department of Electrical and Computer Engineering, Technical University of Munich, Arcisstraße 21, 80333 Munich, Germany*
[2]*Institute of Biomedical Optics, University of Lübeck, Peter-Monnik-Weg 4, 23562 Lübeck, Germany*
*mark.schmidt@tum.de

Abstract: Understanding the dynamics of Fourier domain mode-locked (FDML) lasers is crucial for determining physical coherence limits, and for finding new superior methods for experimental realization. In addition, the rich interplay of linear and nonlinear effects in a laser ring system is of great theoretical interest. Here we investigate the dynamics of a highly dispersion-compensated setup, where over a bandwidth of more than 100 nm, a highly coherent output with nearly shot-noise-limited intensity fluctuations was experimentally demonstrated. This output is called the sweet-spot. We show by numerical simulation that a finite amount of residual dispersion in the fiber delay cavity of FDML lasers can be compensated by the group delay dispersion in the swept bandpass filter, such that the intensity trace exhibits no dips or high-frequency distortions, which are the main source of noise in the laser. In the same way, a small detuning from the ideal sweep filter frequency can be tolerated. Furthermore, we find that the filter's group delay dispersion improves the coherence properties of the laser, and acts as a self-stabilizing element in the cavity. Our theoretical model is validated against experimental data, showing that all relevant physical effects for the sweet-spot operating regime are included.

1. Introduction

Fourier domain mode-locking is a laser operating mode in which a tunable optical bandpass filter is swept synchronously to the roundtrip time of the optical field in the laser cavity. The main components are a rapidly tunable Fabry-Pérot (FP) filter with moving mirrors and a fiber delay line in the order of several hundreds of meters to kilometers. This laser principle has no upper limit to the tuning speed under ideal resonance conditions [1] since the laser remains in single-mode operation. The change in the wavelength in this case is obtained by the Doppler shift, caused by the moving mirror of the FP optical bandpass filter [1,2]. Thus, the laser tuning does not suffer from mode-hopping, which is the major limiting factor in the tuning speed of swept laser systems. FDML lasers have revolutionized optical imaging and sensing techniques, especially optical coherence tomography (OCT) [3–9], and applications in FDML-based Bragg grating sensor systems [10–12] have been realized. Furthermore, real time spectroscopy [13–15], high-speed stimulated Raman scattering spectroscopy [16] and picosecond pulse generation [17] have been demonstrated. The combination of high output powers in the range of 100 mW [18], sweep frequencies of up to 5 MHz [4], typical sweep bandwidths of more than 100 nm and instantaneous linewidths below 0.1 nm [6] make the FDML laser one of the favored systems for tunable lasers. Other important swept-laser sources are vertical-cavity surface emitting lasers with a microelectromechanical system (MEMS-VCSEL) [19,20], and Vernier-tuned distributed Bragg reflector (VT-DBR) lasers [21].

In their normal operation mode, FDML lasers suffer from high intensity noise, with fluctuations of almost 100 % [22]. The intensity fluctuations constitute high-frequency noise compared to the sweep speed of the laser wavelength, and significantly influence the phase stability and coherence

length of the laser. A main limiting factor is considered to be chromatic dispersion in the fiber cavity, which delays or accelerates the instantaneous frequency (IF) of the optical field with respect to the sweep period of the FP filter during each pass through the fiber delay line, and accumulates over consecutive roundtrips unless there is a reverse shift.

A new operating regime discovered by Kraetschmer and Sanders [23], called the sweet-spot, showed shot-noise-limited intensity fluctuations and a significantly narrowed instantaneous linewidth in a 3.5 nm band. This was achieved via a dispersion-compensated setup, with near-perfect synchronization of the sweep frequency to the optical roundtrip time, in the order of a few mHz. This ultra-stable operating mode was recently extended to 117 nm [24] and paves the way towards reaching the coherence limit in FDML lasers. In particular, such low-noise light sources are essential for OCT systems in order to achieve shot-noise-limited detection sensitivity for high-quality images, which has already been observed in former time domain OCT systems [25,26]. It is even more critical in recent swept-source OCT systems, since here not only the system sensitivity but also the maximum ranging depth [24] and the dynamic range [27] can be negatively affected by laser noise.

An understanding of the rich FDML laser dynamics is therefore of fundamental importance for reaching the coherence limit. Here we present a self-stabilization mechanism in a highly dispersion-compensated setup, where a finite remaining dispersion in the fiber delay cavity can be compensated due to the dynamics induced by the frequency-dependent group delay of the swept FP filter. This self-stabilizing effect leads to a tolerance over non-synchronized resonance conditions in the ring laser setup, which ultimately makes sweet-spot operation possible at all. We believe that understanding and controlling this self-stabilization effect can improve FDML frequency combs, which were demonstrated in [28–30], and might enable short pulse generation in the low- or sub-ps range.

The nonlinear system dynamics of FDML lasers has been studied theoretically within different approaches, whereby the problem was modeled as a time-delay dynamical system [31–33] or with the real-valued Ginzburg-Landau equation with a zero group delay (GD) Gaussian filter [34]. Within these approaches, several stability boundaries were derived by a linear stability analysis of stationary solutions, and different operating regimes such as the Turing [32], the Eckhaus [34] or a complex modulation instability [31–33] were discussed. As far as we are aware, none of these investigations refer to a stabilizing mechanism which is due to the dispersive group delay in the FP filter, enabling us to identify a physical mechanism behind the stability boundaries. Furthermore, in [34] it is found that the dispersion causes an accumulative frequency shift which will always drive the laser out of the stability region. Note that in this model, a non-causal Gaussian filter was used which has no frequency-dependent group delay.

In the following, we discuss the laser setup for ultra-stable operation and the underlying physical model. Furthermore, we present the self-stabilization mechanism and validate our model against experimental data.

2.   Laser setup for ultra-stable operation

The FDML laser system investigated here [24] is shown in Fig. 1. It consists of a FP tunable bandpass filter and a single-polarization semiconductor optical amplifier (SOA) gain medium which causes the optical field to have a dominant, linearly polarized component. The polarization controller is therefore used in experiment to manually align the polarization state of the optical field with the SOA gain axis. The fiber delay line is dispersion-shifted by mixing two fibers, a SMF-28 and a HI-1060 fiber, in order to move the zero-dispersion wavelength out of the sweep range. In this case, a chirped fiber Bragg grating (cFBG) can be used in order to compensate for chromatic dispersion which was manually fine-tuned by a temperature gradient. The cFBG serves at the same time as the outcoupling element. The isolator ensures unidirectional lasing and the whole laser is temperature controlled, which is critical for reaching the sweet-spot operation mode

in addition to a high sweep frequency stability. The sweep filter frequency was automatically regulated in order to reach sweet-spot operation and to adjust the laser to environmental changes such as temperature fluctuations or drifts in the local oscillator generating the sweep frequency. Further details can be found in [24].
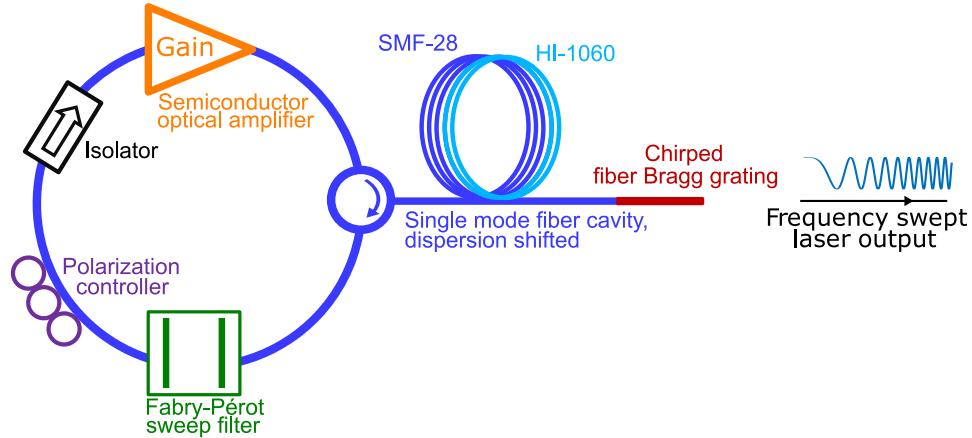

Fig. 1. Schematic illustration of the FDML laser setup for ultra-stable operation.

3. Modeling of ultra-stable operation

The FDML laser dynamics is governed by the field envelope transformations of each of the various components in the laser system. Therefore, we follow a lumped-element approach based on the models in [35] and [36] but with a physical model for the SOA dynamics instead of a phenomenological one. As in our previous investigations of FDML lasers, we use the swept-filter reference frame in which the IF of the optical field is modulated with the center frequency of the sweep filter [35]. Within this approach, the optical field is comoving with the transmission peak of the FP bandpass filter and "sees" a static bandpass filter instead of a swept one. The variations from the peak transmission are thereby contained in the optical field. This approach reduces the simulation bandwidth drastically by three orders of magnitude [35] because the simulation bandwidth is limited by the bandwidth of the sweep filter and not by the whole optical sweep bandwidth. For comparison, a monochromatic field would correspond to a swept field in the reference frame.

The fiber delay cavity including the cFBG modulates the phase of the complex envelope according to

$$u_{\text{out,fiber}}(\tau) = \sqrt{\kappa_{\text{f}}}\, u_{\text{in,fiber}}(\tau) \exp\left\{ iL_{\text{f}}\left[\frac{1}{2}\beta_2\omega_s^2(\tau) + \frac{1}{6}\beta_3\omega_s^3(\tau) + \frac{1}{24}\beta_4\omega_s^4(\tau)\right] + i\varphi_{\text{cFBG}}(\tau) \right.$$
$$\left. + i\gamma\kappa_{\text{f}}|u_{\text{in,fiber}}(\tau)|^2 \frac{1}{2}L_{\text{f}}(1+R) \right\} \tag{1}$$

where L_{f} is the propagation length in the single-mode fiber, β_2 to β_4 are the second- to fourth-order dispersion coefficients, γ is the nonlinearity coefficient of the fiber and κ_{f} accounts for the power loss in the fiber spool, including splicing, circulator as well as fiber losses. For the nonlinear term in the exponential of Eq. (1), κ_{f} is for simplicity fully considered because the exact distribution of losses has not been experimentally characterized. R is the reflectivity of the cFBG. The fiber length L_{f} takes forward and backward propagation after reflection at the

cFBG into account. The center frequency of the swept filter is $\omega_s(\tau) + \omega_c$ with the center frequency of the sweep ω_c where the relative sweep frequency $\omega_s(\tau)$ is chosen here to be $0.5D_\omega \cos(\omega_0\tau)$ with the sweep bandwidth D_ω and the sweep filter tuning frequency ω_0 but can in principle be an arbitrary periodic function. We abbreviate the complex field envelope at the spatial fiber input $u_{\text{in,fiber}}\left(z = z_{\text{in,fiber}}, \tau\right)$, or output $u_{\text{out,fiber}}\left(z = z_{\text{out,fiber}}, \tau\right)$ respectively, with $u_{\text{in,fiber}}(\tau)$ or $u_{\text{out,fiber}}(\tau)$ where we always refer to the spatial input or output position inside the cavity, and drop the z dependence in the following. The cFBG is modeled as an ideal dispersion-compensating element by partially reverting the phase accumulation due to the fiber dispersion by $\varphi_{\text{cFBG}}(\tau) = -L_{\text{f}}\left[(1/2)\hat{\beta}_2\omega_s^2(\tau) + (1/6)\hat{\beta}_3\omega_s^3(\tau) + (1/24)\hat{\beta}_4\omega_s^4(\tau)\right]$. In this way, the dispersion relation of the cFBG needs not be implemented explicitly, but can be included by simply scaling the dispersion coefficients of the optical fiber by $\beta_i - \hat{\beta}_i = \beta_i/c_{\text{scale}}$ with $i \in \{2, 3, 4\}$ and a constant c_{scale} in order to simulate a residual dispersion in the case of non-ideal compensation.

The SOA gain medium modifies the complex field envelope according to

$$u_{\text{out,SOA}}(\tau) = u_{\text{in,SOA}}(\tau)\exp\left\{0.5h(\tau)\left[1 - i\alpha\right]\right\} \tag{2}$$

where $h(\tau) = \int_0^L g(z, \tau)\,dz$ is the integrated power-gain coefficient $g(z, \tau)$ over the length L of the gain medium, and α is the linewidth enhancement factor responsible for self-phase modulation (SPM) in the saturated amplifier. The integrated gain has the dynamics [37]

$$\frac{\partial h(\tau)}{\partial \tau} = \frac{h_0\left[w_s(\tau) + \omega_c\right] - h(\tau)}{\tau_c} - \frac{\left|u_{\text{in,SOA}}(\tau) + u_{\text{ASE}}(\tau)\right|^2}{P_{\text{sat}}\left[w_s(\tau) + \omega_c\right]\tau_c}\left[e^{h(\tau)} - 1\right] \tag{3}$$

with the saturation power P_{sat} and the carrier lifetime τ_c. The amplified spontaneous emission (ASE) noise $u_{\text{ASE}}(\tau)$ is modeled as additive white Gaussian noise with zero mean and effective standard deviation $\sigma = (0.5P_n\Delta_{\text{sim}}/G_{\text{eff}})^{1/2}$. Here P_n is the ASE noise power within the gain bandwidth, $G_{\text{eff}} = \int_0^\infty \exp\left[h_0(f)\right]df$ and Δ_{sim} is the simulation bandwidth. The factor 0.5 accounts for the real and imaginary part of the complex field envelope. Note that the optical field envelope $u(\tau)$ is normalized to the optical power and has the unit $\sqrt{\text{W}}$. The unsaturated static gain $\exp\left[h_0(\omega)\right]$ and the saturation power $P_{\text{sat}}(\omega)$ are frequency-dependent and are modulated in the swept-filter reference frame with the sweep frequency of the filter, which is a good approximation for small deviations of the IF of the optical field from the filter's sweep frequency. The unsaturated gain curve as well as the saturation power were measured (Thorlabs BOA1132S) and are interpolated in the simulation. The frequency dependency of α and τ_c is neglected here, in order to reduce the complexity of the underlying physical model.

As mentioned above, the sweep filter in the swept-filter reference frame is represented by a linear static filter which is treated in the frequency domain [1,35]. With a Lorentzian lineshape of width Δ_ω we obtain for the field transformation of the filter per roundtrip

$$U_{\text{out,FP}}(\omega) = U_{\text{in,FP}}(\omega)H(\omega) \tag{4}$$

where

$$H(\omega) = \frac{\sqrt{T_{\text{max}}}}{1 - i2\omega/\Delta_\omega} \tag{5}$$

and T_{max} is the maximum power-transmission factor.

Polarization effects in the fiber spool are neglected in our model, since the amplifier is a single-polarization device, causing the degenerate orthogonal fiber mode to have a minimal influence on the laser dynamics. However, it should be noted that in principle, a passive stabilization effect due to polarization dynamics could be beneficial for the ultra-stable operating

regime [36]. Furthermore, we do not take into account spectral hole burning or carrier heating in the SOA, since we are only interested in the dominant effects in the gain medium, for the sake of simplicity. Nevertheless, such effects could easily be added in a quasi-static approach.

4. Stability limit for non-synchronized resonance conditions

The ideal laser resonance condition for an FDML laser requires the roundtrip time of the optical field to coincide with the sweep period of the tunable bandpass filter for each instantaneous wavelength of the optical field [1]. Due to the wavelength dependence of the laser components such as fiber dispersion, the frequency-dependent group delay of the optical bandpass filter, or nonlinear frequency shifts arising from SPM in SOA and fiber, this condition cannot be achieved for a constant sweep period unless there exists a frequency-dependent compensation mechanism.

When the laser is operating outside its stability range, a main source of noise in the intensity trace of the laser output are dips (also refered to as holes [22,24]) whose occurrence appears to be irregular. Such hole formations have experimentally been observed in FDML lasers in [33] and are associated with Nozaki-Bekki holes which are spatially localized solutions of the one-dimensional complex Ginzburg-Landau equation [38]. The stability of these holes is sensitive to perturbations and the whole system undergoes bifurcation points, separating stability regions which have complex dependencies. More details are discussed for example in [39,40]. A mathematical proof of whether such a solution is also valid within the FDML laser equations is yet to be provided.

In this work, we find - by numerical simulation - that the laser can operate without holes in the intensity trace within a certain tolerance of either a residual dispersion or a small detuning from the optimal sweep filter frequency. We consider the optimal sweep filter frequency as the inverse of the roundtrip time which is L_f/v_g where L_f is the fiber propagation length and v_g is the group velocity in the fiber, i.e. for an ideal delay fiber, and no delay within the other components. In the absence of other delays, this would result in an optical field with an IF which is zero in the swept-filter reference frame and thus matches the center of the filter transmission function for all times.

4.1. Dispersion compensation

In Fig. 2 the intensity traces for simulations with several amounts of residual dispersion are presented for parameter values given in Table 1. The parameters are selected to be close to the experimental setup described in Section 2, but with a sinusoidal sweep function and neglected switch-on and -off processes in the gain medium resulting from the buffering technique [27,41]. A typical value for the average power at the laser output was measured to be $\approx$ 30 mW and corresponds well with the value obtained in our simulations from Fig. 2(a), i.e. 29 mW for a residual dispersion of 56 or 84 fs respectively. Further information about the implementation is given in Appendix A. The sweet-spot operation mode with a residual fiber dispersion is confirmed in Fig. 2(a) with an ASE noise-limited intensity trace, whereas in Fig. 2(b) the intensity trace is distorted by high-frequency noise. This noise is dominated by consecutive holes and occurs after a threshold of residual dispersion in the fiber system is exceeded. The shape of the holes is described in detail in Section 5. The maximum group delay between the fastest and slowest wavelength caused by the fiber in each roundtrip is given below by the difference between the maximum and minimum value of the fiber cavity group delay $\tau_g(\omega) = L_f \left(\beta_2\omega + \beta_3\omega^2/2 + \beta_4\omega^3/6\right)/c_{\text{scale}}$ and used to quantify the residual dispersion in the fiber cavity.

The threshold after which holes are formed in the intensity trace occurs for the system under investigation at around 100 fs of maximum group delay difference in the fiber within a 117 nm bandwidth.

This phenomenon is demonstrated in Fig. 3(a) which relates the number of holes in the intensity trace to the residual fiber dispersion, and shows the effect of the GD in the FP bandpass filter.
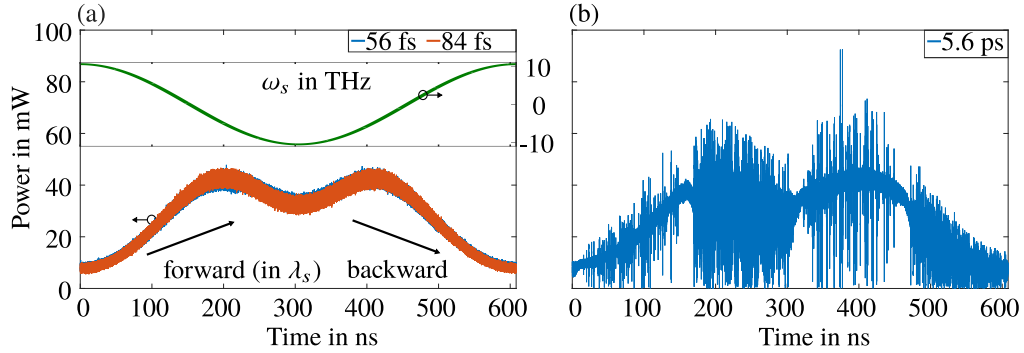
Fig. 2. (a) Simulated intensity trace of a forward and backward sweep in the sweet-spot operation mode with no hole formation, although dispersion is present in the fiber cavity, which is measured as the maximum GD difference due to $\tau_g(\omega)$. Here λ_s is the relative center frequency of the swept FP filter ω_s in respect to wavelength. Note that $\omega_s = 0$ refers to the center frequency ω_c of the sweep. (b) Hole formation beyond a threshold of a finite amount of residual dispersion.

Table 1. Simulation Parameters

Parameter	Symbol	Value
Fiber length	L_f	443.4 m
Fiber group refractive index	n_g	1.645
Second-order dispersion parameter	β_2	9.42×10^{-27} s^2 m^{-1}
Third-order dispersion parameter	β_3	7.62×10^{-41} s^3 m^{-1}
Fourth-order dispersion parameter	β_4	1.70×10^{-55} s^4 m^{-1}
Fiber nonlinearity parameter	γ	2.67×10^{-3} W^{-1} m^{-1}
Power loss in fiber spool	κ_f	0.23
Reflectivity of cFBG	R	0.35
Dispersion coefficients of cFBG	$\hat{\beta}_2,\hat{\beta}_3,\hat{\beta}_4$	variable
Center sweep frequency	ω_c	$2\pi\cdot232.04$ THz (1292 nm)
Sweep bandwidth	D_ω	$2\pi\cdot21.06$ THz (117 nm)
Sweep frequency	ω_0	$2\pi\cdot411$ kHz
Linewidth enhancement factor	α	1.55 [42]
Carrier lifetime	τ_c	70 ps [42]
Simulation bandwidth	Δ_{sim}	3.45 THz
Effective gain	G_{eff}	2.06×10^{16} s^{-1}
ASE noise power in simulation bandwidth	P_n	9.05 mW
FP filter bandwidth	Δ_ω	$2\pi\cdot29.65$ GHz (0.165 nm)
FP filter transmission	T_{max}	0.33
Total cavity losses	L	15.76 dB

Clearly, the presence of the GD in the FP bandpass filter enables hole-free operation up to a fiber dispersion of around 100 fs. The GD in the FP bandpass filter was removed by ignoring the phase shift in the frequency domain, i.e. using $|H(\omega)|$ in Eq. (4). In addition, the average linewidth within a roundtrip in Fig. 3(b) is reduced by more than a factor of two when the GD in the FP bandpass filter is present. For large residual dispersion values and a high-frequency distorted

intensity trace, the linewidth as well as the number of holes of the system with GD is larger than for the system without GD, indicating a negative effect on the stability due to the GD introduced by the FP bandpass filter in this regime.
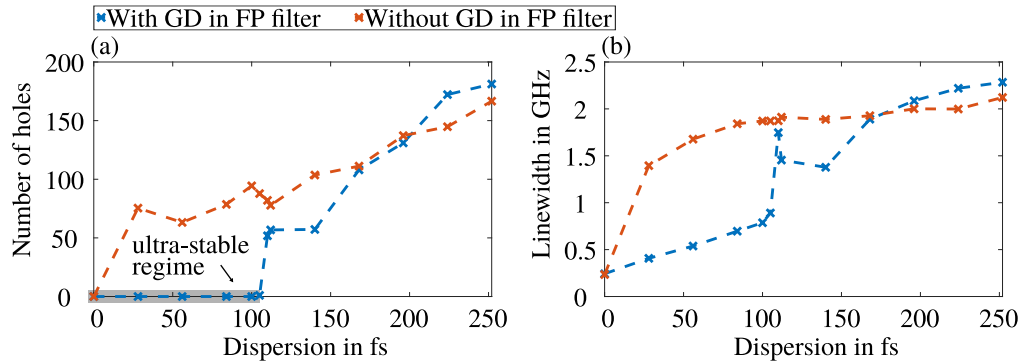

Fig. 3. (a) Number of holes in the intensity trace and (b) the averaged instantaneous linewidth within a roundtrip dependent on the residual dispersion in the fiber delay cavity, compared for the case with and without a GD in the FP bandpass filter.

The results of Fig. 3 prove that a self-stabilizing effect regulates the phase accumulation of the optical field due to the fiber dispersion in the cavity, unless a threshold is exceeded. According to our simulation, a passive mechanism, which identified here as being the frequency-dependent group delay in the FP bandpass filter, plays a major role in this process and is an indispensable requirement for hole-free operation in the sweet-spot regime. A more detailed discussion can be found in Section 4.3. In addition, this self-compensation makes the sweet-spot regime possible in the first place, since perfect synchronization over all wavelengths cannot be achieved in experiment.

The evolution of the IF and the instantaneous lineshape in the sweet-spot operation mode within a single roundtrip is demonstrated in Fig. 4 at the output of the SOA. The position of the IF inside the static bandpass filter window is mainly determined by the dispersion perturbation and is a measure for the delay with regard to the center of the FP bandpass filter. In Fig. 4(a) the IF is extracted for different roundtrip numbers, and selected lineshapes are presented in Fig. 4(b). The lineshapes correspond to the minimum and maximum peak values in Fig. 4(a) and to the middle of the sweep, i.e. the center window of the STFT, of roundtrip 150 000. In the case presented in Fig. 4, a maximum group delay difference of 56 fs is present in the fiber delay cavity as in the case of Fig. 2(a). The variation of the IF is caused by the fiber dispersion which imposes a frequency chirp according to Eq. (1) on the optical field in each roundtrip. As a comparison, the IF evolution in the case of zero-dispersion in the fiber cavity exhibits a nearly straight line (see also Section 4.3) instead of the oscillatory behavior in Fig. 4(a) resulting from the interplay between the FP sweep filter, the SOA gain medium and the fiber dispersion. The drift of the IF over several 1000 roundtrips from Fig. 4(a) is stable within a tolerance of a few GHz, but never converges to a constant value. When looking at the long-term evolution of the averaged instantaneous linewidth over a single roundtrip in Fig. 5(a) a similar drift can be observed over many 10 000 roundtrips, yet the short-term evolution over 100 roundtrips in Fig. 5(b) shows a steady-state behavior. The same can be observed for the IF. The long-term variations can be addressed to the nonlinear nature of the FDML laser, and we have verified in our simulations that the stochastic influence of the ASE noise is amplifying, but does not cause the long-term drift. This long-term drift is supported by experimental data acquired in FDML-based OCT systems where coherent averaging can only be applied up to roughly 100 roundtrips [43], and has also

been observed in previous long-term simulations [36]. Apparently, a stationary field does not exist, but the variations of the IF stay within a few GHz.
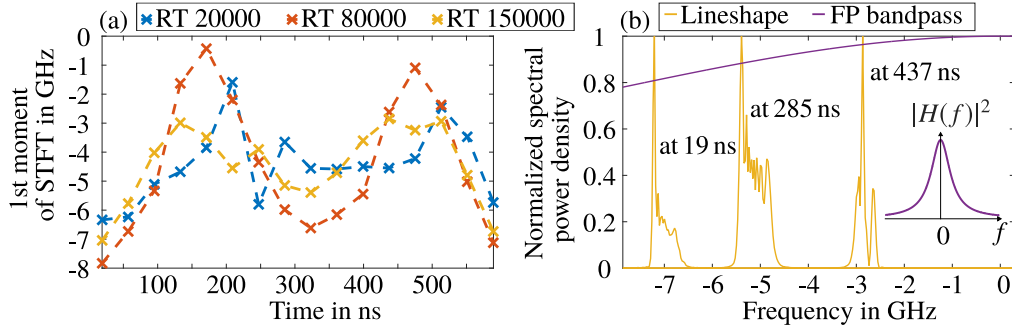
Fig. 4. (a) Evolution of the IF within a single roundtrip for different roundtrip numbers in the sweet-spot regime with a residual dispersion of 56 fs. (b) Instantaneous lineshapes at particular positions in the sweep of roundtrip (RT) 150 000.
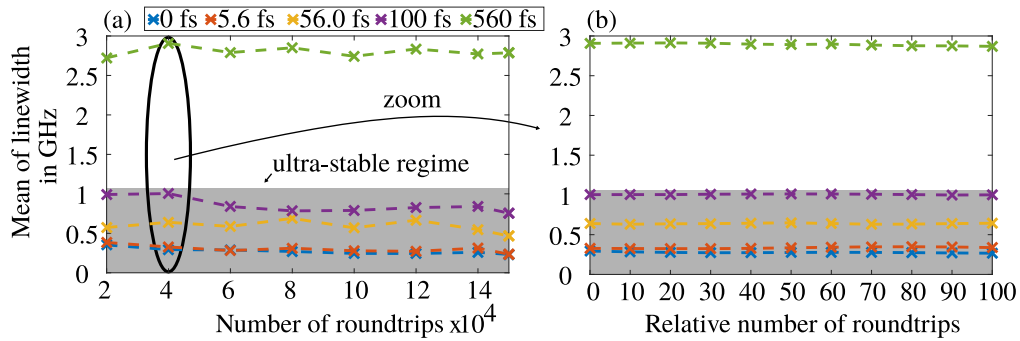
Fig. 5. (a) Long-term evolution of the averaged linewidth within one roundtrip for different amounts of residual dispersion. (b) Short-term evolution of the linewidth showing stationary operation, starting at roundtrip 40000 sampled at every 10th roundtrip.

4.2. Detuning tolerance

When considering a dispersion-less cavity, i.e. $\beta_{2,3,4}, \hat{\beta}_{2,3,4} = 0$, and a non-perfectly synchronized sweep filter, our simulations indicate that a detuning of up to ± 1.0 mHz - equivalent to a change in the roundtrip time of ∓ 5.9 fs from the ideal resonance frequency of 411 kHz - does not cause hole formation in the intensity trace. The compensation mechanism remains the same as discussed in the previous section. This result is consistent with measured data where the laser was detuned from the experimentally obtained sweet-spot operation mode. Here the experimental setup was again buffered [27,41] and a single optical sweep was contained in 300 ns. Asymmetries between the forward and backward sweep have been observed, but are small when enforcing hole-free operation in a dispersion-free setup. The presented value here for the detuning from the ideal sweep frequency is a limit for the backward and forward sweep.

In the swept-filter reference frame, a delayed optical field corresponds to a phase modulation according to

$$u_{\text{out}}(\tau) = u_{\text{in}}(\tau) \exp[i\tau_{\text{d}}\omega_s(\tau)], \qquad (6)$$

where τ_d is the additional delay to the dispersionless roundtrip time and higher-order terms in the temporal derivatives have been neglected, as discussed in Appendix C. Thus, a delay accumulates to the phase of the optical field linearly in $\omega_s(\tau)$ while the dispersion perturbation accumulates quadratically or cubically in $\omega_s(\tau)$ as can be seen in Eq. (6) and Eq. (1).

4.3.   Discussion of the self-stabilization effect

The fiber dispersion and the detuning from the ideal filter frequency introduce timing delays in the optical field relative to the moving transmission window of the swept bandpass filter, i.e. cause a frequency-dependent roundtrip time $RTT(\omega)$.

One quantity to measure the introduced time delays is the IF of the optical field, which describes the offset from the center of the static bandpass filter in the swept-filter reference frame as mentioned above. The shift in the IF caused by the fiber dispersion or by a detuning can be obtained by differentiating the phase of the complex exponential in Eq. (1) or Eq. (6) with respect to time. For example, in the case of the fiber dispersion, this yields

$$\Delta f_{IF} = -1/(2\pi)L_f\omega_s(\tau)\frac{\partial\omega_s(\tau)}{\partial\tau}\left[\beta_2 + \frac{1}{2}\beta_3\omega_s(\tau) + \frac{1}{6}\beta_4\omega_s^2(\tau)\right] \tag{7}$$

per pass through the fiber spool.

An analytic treatment of the self-stabilization mechanism is tedious due to the nonlinear dependencies such as the frequency-dependent GD of the FP filter with respect to frequency, and the complex interplay of the processes in the SOA gain medium, the filter and the fiber over a long time scale. Thus, we focus on an intuitive explanation in the following.

The frequency-dependent GD of the bandpass filter $GD(\omega)$ is able to reduce the roundtrip time for a specific IF when moved away from the center of the filter, where the GD is maximum for a Lorentzian filter shape. The shape of $GD(\omega)$ of the static bandpass filter in the frequency domain is given by

$$GD(\omega) = \frac{2}{\Delta_\omega}\frac{1}{1 + (2\omega/\Delta_\omega)^2}. \tag{8}$$

At $\omega = 0$, in the center of the bandpass filter, the GD is 10.7 ps and always less when $|\omega|>0$, e.g. reduced by 730 fs when shifted by -4 GHz. In this way, a delayed IF with respect to the center of the filter can be accelerated over consecutive roundtrips to a position in the filter window where no holes form within the threshold limit, whereas an accelerated IF would be further accelerated, leading to an unstable drift. Related further discussion can be found in [24]. The selection of the stable filter position depends on the amount of residual dispersion in the fiber as discussed above and is demonstrated in Fig. 6(a). Here, it is evident that the IF chooses a different position in the filter window dependent on the fiber dispersion, in order to operate in the sweet-spot regime. In comparison, when the bandpass filter has no GD in Fig. 6(b) the IF does not differ significantly with different amounts of dispersion in the fiber cavity, and holes are formed as demonstrated in Fig. 3(a). One important factor is here that the modified roundtrip times are not compensated for. For the case of 5.6 ps, the intensity trace is distorted by high-frequency noise as presented in Fig. 2(b), and in Fig. 6(a), the evolution of the IF follows the fiber chirp Δf_{IF} which is depicted below, when taking the zero-dispersion line as a reference. The same holds for the case without GD in the FP filter. Again this shows that the accumulated chirp per roundtrip due to the fiber dispersion cannot be compensated in these cases. Yet, single narrow sweet-spots exist when crossing the zero-dispersion line, see Fig. 2(b).

Another important feature of the self-stabilization effect is the temporal extension over several thousands of roundtrips until the quasi-steady-state regime of Fig. 6(a) is reached. This can be demonstrated by starting with zero-dispersion in the fiber cavity and abruptly switching on the fiber dispersion after 10 000 roundtrips. In Fig. 7(a) this scenario is shown for a residual
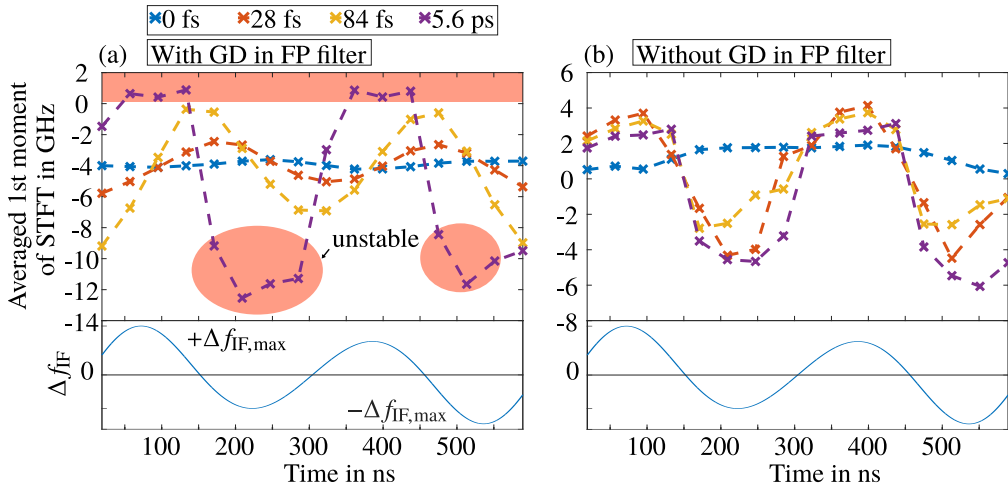
Fig. 6. (a) IF evolution for different amounts of residual dispersion at the output of the SOA. (b) The same as in (a) but with no GD in FP bandpass filter.

dispersion of 100 fs where the maximum shift in the IF is $\Delta f_{\text{IF,max}} = \pm 3.6$ MHz per roundtrip. Note that in the case of 100 fs the long-term drift of the IF as discussed in Fig. 4(a) for 56 fs is far less pronounced. In the first few hundred roundrips the IF follows the dispersion accumulation in the fiber as visualized in Fig. 7(b) where the solid lines are obtained from $n\Delta f_{\text{IF}}(\tau_w)$ with the roundtrip number n and the temporal center of the STFT window τ_w. In a single roundtrip, this shift in the IF is equivalent to a change in the roundtrip time. The difference in $GD(\omega)$ in the FP filter between the zero-dispersion position of approximately -4 GHz shifted by -3.6 MHz is ≈ 1 fs and thus negligible compared to the delays introduced by the dispersion. Yet, during the long-term accumulation, this difference increases to ≈ 800 fs when shifted by -2 GHz, which exceeds the maximum dispersion delay by a factor of 8. Hence, the frequency offset required for the compensation due to the group delay of the FP filter builds up over many roundtrips.
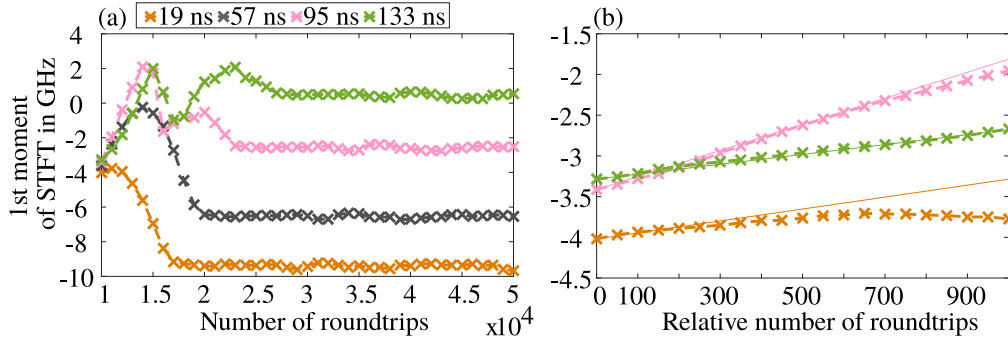
Fig. 7. (a) Long-term drift of the IF at specific points in time or equivalently of single wavelengths over 40 000 roundtrips when switching on a fiber dispersion of 100 fs after 10 000 roundtrips until the quasi-steady-state is reached. (b) Zoom into the first 1000 roundtrips compared to the dispersion accumulation in the fiber (solid line).

Based on our findings, it can be speculated that by engineering the GD in the FP filter by e.g. using chirped dielectric coatings on the FP filter mirrors or modifying the filter bandwidth, the

system can be made more robust against residual fiber dispersion or environmental changes. An increase in the stability threshold found in Section 4.1 could enable a widespread use of the ultra-stable operating regime, which requires up to now a high level of synchronization. The model presented here serves as an ideal starting point for such optimization problems.

4.4.   Influence of SOA parameters on the sweet-spot operation mode

The carrier lifetime τ_c, the linewidth enhancement factor α and the saturation power P_{sat} of the SOA gain medium play an important role in obtaining the sweet-spot operation mode. Especially the phase accumulation due to the linewidth enhancement factor in combination with the gain recovery dynamics and the interplay with the swept FP filter can create chaotic intensity traces. With typical values of $\tau_c = 380\,\mathrm{ps}$ and $\alpha = 5$ as previously used in [35,36] a sweet-spot operation mode could not be achieved. An InP/InGaAsP multiple-quantum-well (MQW) booster SOA was used in [24] (Thorlabs BOA1132S) whose physical properties at the corresponding operating condition need to be known. Yet, to the best of our knowledge, no rigorous characterization of α exists in the specific wavelength range of interest for this device. It is commonly known that strained MQW structures exhibit a reduced linewidth enhancement factor due to the high differential gain compared to bulk materials [44–47], and values of $\alpha \leq 2$ were reported for the same wavelength and material system for lasers. Similarly, the SOA here serves as the laser gain medium, and essentially compensates for the roundtrip losses, thus operating in the saturated regime. Dynamical aspects, similar to SOAs for signal amplification, come into play for the hole formation in FDML lasers. In this case, the literature values found for α are far more diverse, with some references stating similar values as above [48–50] and others reporting values of 3 or higher for various devices and operating conditions [51–57]. When using the parameters $\tau_c = 440\,\mathrm{ps}$, $\alpha = 3$ from a study of SOA fiber ring lasers with a static bandpass filter [58], a sweet-spot over the whole sweep bandwidth is found in our simulation. However, at moderate dispersion levels, fringes occur in the hole minima which cannot be observed in experiment, as will be discussed in the section below. Therefore, we conclude that the above lower α value, as reported for strained MQW laser operation, yields the best agreement with the shape and time scale of the holes in experiment, especially at moderate dispersion levels. Further simulations reveal that a shorter carrier lifetime combined with a higher α factor increases the occurrence of fringes in the holes. In [59], it was discussed that a time-dependent α-factor which also depends on the carrier density and wavelength might be more adequate for accurately modeling highly dynamic processes in the order of ps. However, due to the numerical load of our simulations and the intention to derive a compact model suitable for optimization purposes, this approach will be left to future work. On the other hand, carrier heating and spectral hole burning have been found to be negligible at the time scale of the holes [53,59,60].

5.   Experimental verification

In order to verify our physical model, we reproduced a detuned intensity trace of an FDML laser with a non-dispersion-compensated SMF-28 fiber featuring the full noise dynamics due to the dispersion perturbation. The fiber parameters and the dispersion coefficients were extracted from the manufacturer specification [61]. The measured intensity trace of a backward sweep of 104 nm centered around 1307 nm is shown in Fig. 8(a). The bandpass filter was driven with a frequency of 363 kHz which was slightly detuned from the sweep frequency where the center wavelength matches the roundtrip time in the laser cavity, resulting in a noisy intensity trace with a single narrow sweet-spot around the middle of the sweep. In the detuned case, two narrow sweet-spots can be found in the intensity trace, in Fig. 8(a) at around 75 ns and 260 ns, because of the parabolically shaped dispersion relation which causes two wavelengths to be synchronized to the filter sweep rate. The measurement was obtained with a real-time oscilloscope and a high-speed photodiode, with a total analog bandwidth of 50 GHz.
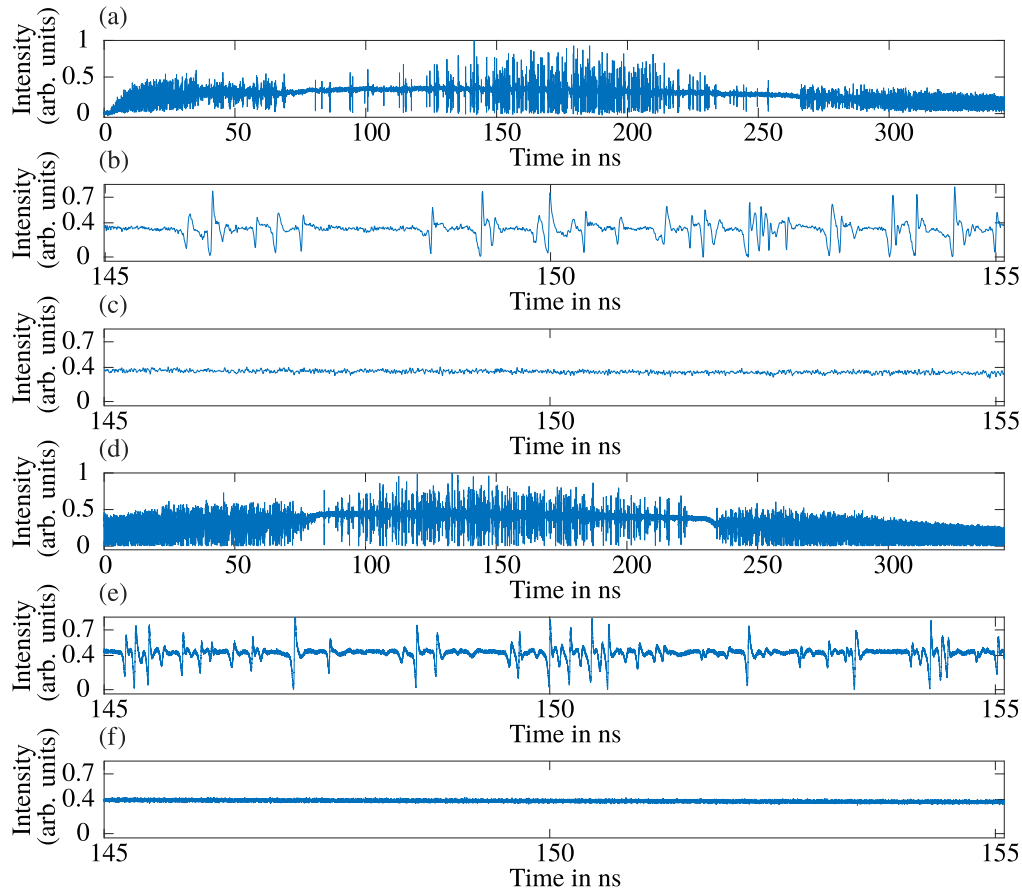
Fig. 8. (a) Measured intensity trace of a laser with a non-dispersion-compensated SMF-28 fiber cavity. The backward sweep of 104 nm is centered around 1307 nm at a filter sweep frequency of 363 kHz. (b) Zoom into a noisy region in the intensity trace, showing the hole dynamics. (c) Identical zoom into the experimentally obtained sweet-spot. (d) A simulated intensity trace of the case in (a) and (e) zoom into noisy region for comparison. (f) Zoom into the sweet-spot with a residual dispersion of 84 fs.

The hole dynamics can be observed in Fig. 8(b) where a 10 ns section around 150 ns is cut out. The characteristic shape of the holes can be identified as a power drop of up to 100 % followed by an overshoot caused by the gain-recovery dynamics in the SOA gain medium. The duration of the holes is, among other things, influenced by the carrier lifetime τ_c of the SOA, as well as the linewidth enhancement factor α, and is in the range of 50 ps to 70 ps.

The reproduced intensity trace, i.e. $|u(\tau)|^2$, at the laser output after 40 000 roundtrips is shown in Figs. 8(d) and (e) respectively. Because of the quasi-stationary nature of the FDML laser, the exact position and shape of the holes can barely be captured in the simulation. Thus, the focus lies here in a qualitative agreement, where we pay special attention to the characteristics of the individual holes. The laser was detuned by −0.8 Hz to obtain the closest match. All in all, good agreement between the simulated and experimental traces can be observed with regard to the hole densities and shapes. Since the switch-on and -off process in the SOA gain medium in the buffering mode is not considered in the simulation, the left and right edges up to 20 ns cannot be compared. This effect has no influence on the physical mechanism behind the self-stabilization,

and is therefore neglected. Figures 9(a) and (b) demonstrate that single holes can be precisely reproduced with the chosen SOA parameters from Table 1. For $\tau_c = 440$ ps and $\alpha = 3$ [58] the hole duration increases by a factor of 2, see Fig. 9(c). Furthermore, in intensity traces with only few holes, special patterns emerge with up to a factor of 10 increased hole durations and fringe formation in the minima, see Fig. 9(d). Such a feature has not been observed in any measured intensity trace. This indicates the sensitivity of the hole dynamics on the SOA parameters and confirms that a carrier lifetime of ≈ 100 ps along with a linewidth enhancement factor $\alpha \approx 1.5$ are a reasonable choice in our case. This is of particular importance, since due to the strong phase-amplitude coupling caused by the narrow sweep filter, a hole contains information about the interplay of all cavity elements as well as the gain recovery dynamics which is visible in the overshoot. The number of holes in the intensity trace was compared in a region between the two narrow sweet-spots from 80 ns to 230 ns where the hole density is moderate. 356 and 315 holes were counted in experiment and in the simulation respectively, which corresponds to a deviation of 12 % and is plausible when considering the above-mentioned uncertainties.
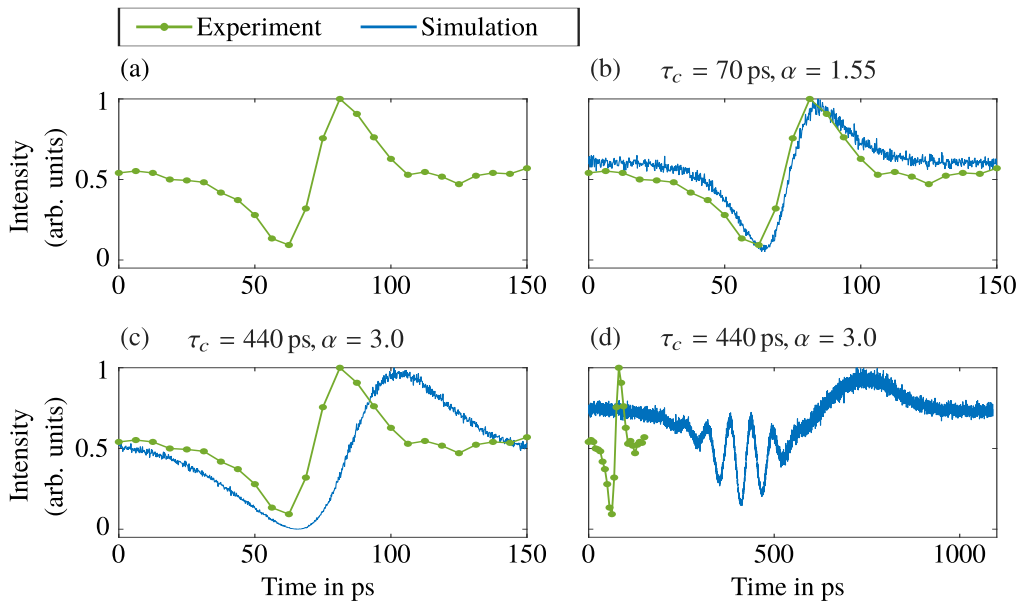
Fig. 9. (a) Measured hole in a laser setup which was detuned by -100 mHz from the ultra-stable regime. (b) A hole extracted from simulation with the SOA parameters used in this work, see Table 1. (c) Hole for the SOA parameters from [58], yet with a longer duration than in the experiment. (d) Fringe-distorted hole for the SOA parameters in (c) which could not be observed in experimentally measured intensity traces.

The good agreement between simulation and experiment shows that all relevant physical mechanisms are contained in our model. Neglecting polarization effects, such as bending-induced birefringence or polarization-mode dispersion in the optical fiber, appears to be a legitimate assumption for a single-polarization SOA, where only a single-polarization component experiences considerable gain. In experiment, a polarization controller before the SOA is used in order to adjust the polarization state of the light field to the axis where the polarization-dependent SOA has maximum gain, and to minimize timing delays introduced by the polarization dynamics. Previous investigations into the polarization state of FDML lasers with a single-polarization SOA operating far beyond the sweet-spot regime showed a well-defined polarization state over the whole sweep bandwidth [62]. This also agrees with the observation in experiment in the

sweet-spot regime that the polarization state of the light field reproduces after each roundtrip at the entrance of the SOA, and does not significantly vary or cause instabilities.

In the case of the numerical simulations described in Section 4.1, the SMF-28 fiber was replaced by the 1 : 8 mix of a SMF-28 and a HI-1060 [63] fiber as discussed above. For both fiber cavities, Turing-like instabilities which are discussed in [32] were observed in parts of the intensity trace in the case of detuning or residual dispersion, along with oscillatory and irregular patterns. This indicates that the hole dynamics can differ in particular cases, typically near the turning point of the sweep filter waveform, in view of the forms seen in Figs. 8(b) and (e). In general, the occurrence of intensity patterns is not stationary over consecutive roundtrips.

6. Conclusion

We have demonstrated by numerical simulation of an FDML laser that a residual dispersion in the fiber cavity which delays or accelerates each instantaneous frequency of the optical field relative to the FP sweep filter can be compensated by the frequency-dependent group delay in the swept bandpass filter, such that no holes occur in the intensity trace of the laser.

Systems without this self-compensation mechanism show less coherence and exhibit a hole-distorted intensity trace because the dispersion perturbation accumulates within each roundtrip without compensation, and drives the system out of its stability region. For the same reason a detuning from the ideal sweep filter frequency of up to ± 1.0 mHz can be regulated for the system of investigation with no dispersion in the optical fiber. Our simulations display good correspondence with experimental data, and show that in a single-polarization setup, the hole dynamics is determined by the complex interplay of the dispersive fiber, the swept bandpass filter and the nonlinear dynamics of the SOA gain medium.

Within the sweet-spot regime, the generation of FDML-based frequency combs is highly attractive, and the temporal compression limit of the wavelength-swept laser output for short pulse generation may be reached, which is in the sub-ps range [17]. This ultra-stable operating regime with its enhanced coherence properties offers new, unexplored possibilities in sensing and imaging applications.

Appendix A: Additional implementation information

1. Fiber

The fiber delay line consists of a 1 : 8 mix of a SMF-28 [61] and a HI-1060 [63] fiber to shift the zero-dispersion wavelength out of the sweep window such that the cFBG can be used for dispersion compensation. Here, we used a model for the dispersion coefficient β_2 of the SMF-28 fiber provided by the manufacturer [61] which was fitted to the experimentally obtained dispersion-relation of the fiber mix. Thus, adapted values were used for the fiber length (443.4 m), the zero-dispersion wavelength (1418.9 nm) and the zero-dispersion slope (0.07 ps nm^{-2} km^{-1}) which are required for the manufacturer's model. In addition, this model was verified experimentally.

2. Buffering

The experimental laser curve was recorded in the buffered mode [27,41] when the laser is run in a 1/8 duty cycle in order to increase the sweep frequency by copying single sweeps of the optical field, after out-coupling the light from the cavity. In this way, the sweep rate can be increased by increasing the amplitude of the FP sweep filter drive function without increasing its mechanical resonance frequency, which constitutes a bottleneck for the maximum FDML sweep rate [4]. In the simulation, the off-time of 7/8 of the sweep was not considered. Instead, we used the physical fiber length of 443.4 m (562.6 m in Section 5) in Eq. (1) and replaced the corresponding sweep rate of 411 kHz (363 kHz) by $8 \cdot 411$ kHz ($8 \cdot 363$ kHz) for a single sweep. In doing so, we obtained a continuous sweep with the correct sweep timings and the actual physical propagation

length in the cavity. However, we neglected the switch-on and -off process in the SOA due to the continuous sweep, as well as the off-time, which carries no relevant physical information. The good agreement in Section 5 validates this approach.

Because of the buffering technique, the sweep of the bandpass filter is nearly linear since only at 1/8 of the sweep time around the zero crossing point of the sinusoidal sweep function is the gain medium switched on. A linear sweep function was therefore used in Section 5.

3. SOA

Equation (3) was numerically integrated with a fourth-order Runge-Kutta method. The unsaturated gain was interpolated with a Gaussian and the saturation power with a fourth-order polynomial. Note that the measured input saturation power $P_{sat,m,in}$ is related with P_{sat} in Eq. (3) by $P_{sat} = [\exp(h_0) - 2]/[2\log(2)]P_{sat,m,in}$.

Appendix B: Characterization of the ultra-stable operating regime

In order to quantify the coherence properties of the ultra-stable operating regime, we determine the width of the instantaneous lineshape and the number of local minima of the high-frequency fluctuations in the intensity trace, i.e the number of holes. The instantaneous lineshape is a local measure of the phase evolution and of fluctuations in the optical field, whereas the high-frequency noise in the intensity trace is a result of the complex laser dynamics evolving over many roundtrips. In addition, we describe the optical field by its IF, which measures the offset from the center frequency of the bandpass filter in the swept-filter reference frame. The three above-mentioned quantities are especially important for the imaging properties of FDML lasers [24].

We extract the instantaneous linewidth and frequency by performing a short-time Fourier transformation (STFT) of the complex field envelope, where we use a rectangular window function and divide a single sweep into 16 pieces. For the parameter values chosen here, this corresponds to a minimum theoretical time-frequency uncertainty of 2.09 MHz or 38.02 ns respectively for $T = 608.27$ ns when neglecting the broadening due to the rectangular window. A similar approach was followed in [64,65] where it proved possible to reproduce experimental measurements of the instantaneous laser lineshape. The IF is estimated by the first moment within the STFT window, and the linewidth is estimated by the root mean square bandwidth (RMS) around the mean frequency. The RMS is used here since the lineshape can have different appearances with e.g. a noisy multi-peak structure where a full width at half maximum (FWHM) approach would be inappropriate, and was also used in [58] to characterize SOA fiber ring lasers with a static bandpass filter which are similar to FDML lasers. The blurring effect of noise on the RMS bandwidth was reduced here by using a rectangular window of 30 GHz centered around the peak frequency of the lineshape which is sharply concentrated around the IF, as can be seen in Fig. 4(b).

The number of holes is determined by counting the local minima exceeding a threshold of 30 % from the mean of the intensity trace, obtained by applying a Gaussian low-pass filter with a FWHM width of 100 MHz. To be robust against noise, the minimum peak distance was chosen to be 40 ps and the minimum peak width was set to 5 ps. Furthermore, we limited the bandwidth of the simulated intensity traces with a Gaussian low-pass filter with a FWHM width of 500 GHz, in order to reduce the influence of the ASE noise on the hole counting algorithm.

The IF in Fig. 6 at each computed point was averaged over a period from roundtrips 40 000 to 150 000, sampled every 20 000th roundtrip in order to smooth the drift of the IF which was discussed in Fig. 4(a). The number of holes in Fig. 3(a) as well as the mean linewidth per roundtrip in Fig. 3(b) were averaged in the same way, though starting at roundtrip 100 000, since we observed that certain low amplitude patterns in the intensity trace get smoothed out over this long time scale.

Appendix C: Delay in the swept-filter reference frame

The transformation of the optical field envelope $A(\tau)$ with the retarded time τ to the swept-filter reference frame envelope $u(\tau)$ [35] is performed by

$$u(\tau) = A(\tau) \exp[i\varphi(\tau)]. \tag{9}$$

Here,

$$\varphi(\tau) = \int [\Omega(\tau') - \omega_c] \, d\tau' \tag{10}$$

which modulates the IF of the optical field in accordance with the center frequency of the optical bandpass filter $\Omega(\tau')$, shifted by the center frequency of the sweep ω_c. In the case when the optical field is delayed by a time τ_d the delayed field in the swept-filter reference frame is

$$u_d(\tau) = A(\tau - \tau_d) \exp[i\varphi(\tau)]. \tag{11}$$

The delayed field envelope can be rewritten in terms of $A(\tau)$ as

$$A(\tau - \tau_d) = \sum_{k=0}^{\infty} \frac{\left(-\tau_d \frac{\partial}{\partial \tau}\right)^k}{k!} A(\tau), \tag{12}$$

which follows from the Fourier transform properties, and is known as the time-delay operator $\exp\left(-\tau_d \frac{\partial}{\partial \tau}\right)$. When using the property of Eq. (12) and neglecting higher order time derivatives of $A(\tau)$ as in [35,36] according to

$$\left(\frac{\partial}{\partial \tau}\right)^j A(\tau) \approx [-i\omega_s(\tau)]^j u(\tau) \exp[-i\varphi(\tau)] \tag{13}$$

with $\omega_s(\tau) = \Omega(\tau) - \omega_c$, we obtain

$$u_d(\tau) = \left[\sum_{k=0}^{\infty} \frac{\left(-\tau_d \frac{\partial}{\partial \tau}\right)^k}{k!} A(\tau) \right] \exp[i\varphi(\tau)] \tag{14}$$

$$= \left[A(\tau) + (-\tau_d) \frac{\partial}{\partial \tau} A(\tau) + \frac{(-\tau_d)^2}{2!} \frac{\partial^2}{\partial \tau^2} A(\tau) + \cdots \right] \exp[i\varphi(\tau)] \tag{15}$$

$$= u(\tau) + (-\tau_d)[-i\omega_s(\tau)] u(\tau) + \frac{(-\tau_d)^2}{2!} [-i\omega_s(\tau)]^2 u(\tau) + \cdots \tag{16}$$

$$= u(\tau) \left[1 - i(-\tau_d)\omega_s(\tau) + \frac{[-i(-\tau_d)\omega_s(\tau)]^2}{2!} + \cdots \right] \tag{17}$$

$$= u(\tau) \exp[-i(-\tau_d)\omega_s(\tau)]. \tag{18}$$

Disclosures

TP: Optores GmbH (E,P,R), RH: Optores GmbH (I,P,R), Optovue Inc. (P,R), Zeiss Meditec (P,R), Abott (P,R).

References

1. C. Jirauschek and R. Huber, "Wavelength shifting of intra-cavity photons: Adiabatic wavelength tuning in rapidly wavelength-swept lasers," Biomed. Opt. Express **6**(7), 2448–2465 (2015).
2. A. E. Siegman, *Lasers* (University Science Books, 1986).
3. D. Huang, E. A. Swanson, C. P. Lin, J. S. Schuman, W. G. Stinson, W. Chang, M. R. Hee, T. Flotte, K. Gregory, C. A. Puliafito, and J. G. Fujimoto, "Optical coherence tomography," Science **254**(5035), 1178–1181 (1991).
4. W. Wieser, B. R. Biedermann, T. Klein, C. M. Eigenwillig, and R. Huber, "Multi-megahertz OCT: High quality 3D imaging at 20 million A-scans and 4.5 GVoxels per second," Opt. Express **18**(14), 14685–14704 (2010).
5. B. R. Biedermann, W. Wieser, C. M. Eigenwillig, G. Palte, D. C. Adler, V. J. Srinivasan, J. G. Fujimoto, and R. Huber, "Real time en face Fourier-domain optical coherence tomography with direct hardware frequency demodulation," Opt. Lett. **33**(21), 2556–2558 (2008).
6. D. C. Adler, W. Wieser, F. Trepanier, J. M. Schmitt, and R. A. Huber, "Extended coherence length Fourier domain mode locked lasers at 1310 nm," Opt. Express **19**(21), 20930–20939 (2011).
7. L. Reznicek, T. Klein, W. Wieser, M. Kernt, A. Wolf, C. Haritoglou, A. Kampik, R. Huber, and A. S. Neubauer, "Megahertz ultra-wide-field swept-source retina optical coherence tomography compared to current existing imaging devices," Graefe's Arch. Clin. Exp. Ophthalmol. **252**(6), 1009–1016 (2014).
8. T. Klein, R. André, W. Wieser, T. Pfeiffer, and R. Huber, "Joint aperture detection for speckle reduction and increased collection efficiency in ophthalmic MHz OCT," Biomed. Opt. Express **4**(4), 619–634 (2013).
9. B. R. Biedermann, W. Wieser, C. M. Eigenwillig, and R. Huber, "Recent developments in Fourier Domain Mode Locked lasers for optical coherence tomography: Imaging at 1310 nm vs. 1550 nm wavelength," J. Biophotonics **2**(6-7), 357–363 (2009).
10. E. J. Jung, C.-S. Kim, M. Y. Jeong, M. K. Kim, M. Y. Jeon, W. Jung, and Z. Chen, "Characterization of FBG sensor interrogation based on a FDML wavelength swept laser," Opt. Express **16**(21), 16552–16560 (2008).
11. B. C. Lee and M. Y. Jeon, "Remote fiber sensor based on cascaded Fourier domain mode-locked laser," Opt. Commun. **284**(19), 4607–4610 (2011).
12. B. C. Lee, E.-J. Jung, C.-S. Kim, and M. Y. Jeon, "Dynamic and static strain fiber Bragg grating sensor interrogation with a 1.3 μm Fourier domain mode-locked wavelength-swept laser," Meas. Sci. Technol. **21**(9), 094008 (2010).
13. L. A. Kranendonk, X. An, A. W. Caswell, R. E. Herold, S. T. Sanders, R. Huber, J. G. Fujimoto, Y. Okura, and Y. Urata, "High speed engine gas thermometry by Fourier-domain mode-locked laser absorption spectroscopy," Opt. Express **15**(23), 15115–15128 (2007).
14. L. A. Kranendonk, R. J. Bartula, and S. T. Sanders, "Modeless operation of a wavelength-agile laser by high-speed cavity length changes," Opt. Express **13**(5), 1498–1507 (2005).
15. L. A. Kranendonk, R. Huber, J. G. Fujimoto, and S. T. Sanders, "Wavelength-agile H_2O absorption spectrometer for thermometry of general combustion gases," Proc. Combust. Inst. **31**(1), 783–790 (2007).
16. S. Karpf, M. Eibl, W. Wieser, T. Klein, and R. Huber, "A time-encoded technique for fibre-based hyperspectral broadband stimulated Raman microscopy," Nat. Commun. **6**(1), 6784 (2015).
17. C. M. Eigenwillig, W. Wieser, S. Todor, B. R. Biedermann, T. Klein, C. Jirauschek, and R. Huber, "Picosecond pulses from wavelength-swept continuous-wave Fourier domain mode-locked lasers," Nat. Commun. **4**(1), 1848 (2013).
18. Y. Mao, C. Flueraru, S. Sherif, and S. Chang, "High performance wavelength-swept laser with mode-locking technique for optical coherence tomography," Opt. Commun. **282**(1), 88–92 (2009).
19. P. Qiao, K. T. Cook, K. Li, and C. J. Chang-Hasnain, "Wavelength-swept VCSELs," IEEE J. Sel. Top. Quantum Electron. **23**(6), 1–16 (2017).
20. B. Potsaid, V. Jayaraman, J. G. Fujimoto, J. Jiang, P. J. Heim, and A. E. Cable, "MEMS tunable VCSEL light source for ultrahigh speed 60kHz-1MHz axial scan rate and long range centimeter class OCT imaging," in *Optical Coherence Tomography and Coherence Domain Optical Methods in Biomedicine XVI*, vol. 8213 (International Society for Optics and Photonics, 2012), p. 82130M.
21. M. Bonesi, M. Minneman, J. Ensher, B. Zabihian, H. Sattmann, P. Boschert, E. Hoover, R. Leitgeb, M. Crawford, and W. Drexler, "Akinetic all-semiconductor programmable swept-source at 1550 nm and 1310 nm with centimeters coherence length," Opt. Express **22**(3), 2632–2655 (2014).
22. T. Pfeiffer, W. Draxinger, W. Wieser, T. Klein, M. Petermann, and R. Huber, "Analysis of FDML lasers with meter range coherence," in *Optical Coherence Tomography and Coherence Domain Optical Methods in Biomedicine XXI*, vol. 10053 (International Society for Optics and Photonics, 2017), p. 100531T.
23. T. Kraetschmer and S. T. Sanders, "Ultrastable Fourier domain mode locking observed in a laser sweeping 1363.8 – 1367.3 nm," in *Conference on Lasers and Electro-Optics*, (Optical Society of America, 2009), p. CFB4.
24. T. Pfeiffer, M. Petermann, W. Draxinger, C. Jirauschek, and R. Huber, "Ultra low noise Fourier domain mode locked laser for high quality megahertz optical coherence tomography," Biomed. Opt. Express **9**(9), 4130–4148 (2018).
25. I. Hartl, X. D. Li, C. Chudoba, R. K. Ghanta, T. H. Ko, J. G. Fujimoto, J. K. Ranka, and R. S. Windeler, "Ultrahigh-resolution optical coherence tomography using continuum generation in an air–silica microstructure optical fiber," Opt. Lett. **26**(9), 608–610 (2001).
26. N. Nishizawa, Y. Chen, P. Hsiung, E. P. Ippen, and J. G. Fujimoto, "Real-time, ultrahigh-resolution, optical coherence tomography with an all-fiber, femtosecond fiber laser continuum at 1.5 μm," Opt. Lett. **29**(24), 2846–2848 (2004).
27. R. Huber, D. C. Adler, and J. G. Fujimoto, "Buffered Fourier domain mode locking: unidirectional swept laser sources for optical coherence tomography imaging at 370,000 lines/s," Opt. Lett. **31**(20), 2975–2977 (2006).

28. T.-H. Tsai, C. Zhou, D. C. Adler, and J. G. Fujimoto, "Frequency comb swept lasers," Opt. Express **17**(23), 21257–21270 (2009).

29. M. Wan, F. Li, X. Feng, X. Wang, Y. Cao, B.-O. Guan, D. Huang, J. Yuan, and P. K. A. Wai, "Time and Fourier domain jointly mode locked frequency comb swept fiber laser," Opt. Express **25**(26), 32705–32712 (2017).

30. N. Lippok, M. Siddiqui, B. J. Vakoc, and B. E. Bouma, "Extended coherence length and depth ranging using a Fourier-domain mode-locked frequency comb and circular interferometric ranging," Phys. Rev. Appl. **11**(1), 014018 (2019).

31. A. Pimenov, S. Slepneva, G. Huyet, and A. G. Vladimirov, "Dispersive time-delay dynamical systems," Phys. Rev. Lett. **118**(19), 193901 (2017).

32. S. Slepneva, B. Kelleher, B. O'Shaughnessy, S. P. Hegarty, A. G. Vladimirov, and G. Huyet, "Dynamics of Fourier domain mode-locked lasers," Opt. Express **21**(16), 19240–19251 (2013).

33. S. Slepneva, B. O'Shaughnessy, A. G. Vladimirov, S. Rica, E. A. Viktorov, and G. Huyet, "Convective Nozaki-Bekki holes in a long cavity OCT laser," Opt. Express **27**(11), 16395–16404 (2019).

34. F. Li, K. Nakkeeran, J. N. Kutz, J. Yuan, Z. Kang, X. Zhang, and P. K. A. Wai, "Eckhaus instability in the Fourier-domain mode locked fiber laser cavity," arXiv preprint arXiv:1707.08304 (2017).

35. C. Jirauschek, B. Biedermann, and R. Huber, "A theoretical description of Fourier domain mode locked lasers," Opt. Express **17**(26), 24013–24019 (2009).

36. C. Jirauschek and R. Huber, "Efficient simulation of the swept-waveform polarization dynamics in fiber spools and Fourier domain mode-locked (FDML) lasers," J. Opt. Soc. Am. B **34**(6), 1135–1146 (2017).

37. G. P. Agrawal and N. A. Olsson, "Self-phase modulation and spectral broadening of optical pulses in semiconductor laser amplifiers," IEEE J. Quantum Electron. **25**(11), 2297–2306 (1989).

38. N. Bekki and K. Nozaki, "Formations of spatial patterns and holes in the generalized Ginzburg-Landau equation," Phys. Lett. A **110**(3), 133–135 (1985).

39. H. Chaté and P. Manneville, "Stability of the Bekki-Nozaki hole solutions to the one-dimensional complex Ginzburg-Landau equation," Phys. Lett. A **171**(3-4), 183–188 (1992).

40. H. Chaté, "Spatiotemporal intermittency regimes of the one-dimensional complex Ginzburg-Landau equation," Nonlinearity **7**(1), 185–204 (1994).

41. J. P. Kolb, T. Klein, M. Eibl, T. Pfeiffer, W. Wieser, and R. Huber, "Megahertz FDML laser with up to 143nm sweep range for ultrahigh resolution OCT at 1050nm," in *Optical Coherence Tomography and Coherence Domain Optical Methods in Biomedicine XX*, vol. 9697 (International Society for Optics and Photonics, 2016), p. 969703.

42. D. Cassioli, S. Scotti, and A. Mecozzi, "A time-domain computer simulator of the nonlinear response of semiconductor optical amplifiers," IEEE J. Quantum Electron. **36**(9), 1072–1080 (2000).

43. T. Pfeiffer, W. Wieser, T. Klein, M. Petermann, J.-P. Kolb, M. Eibl, and R. Huber, "Flexible A-scan rate MHz OCT: Computational downscaling by coherent averaging," in *Optical Coherence Tomography and Coherence Domain Optical Methods in Biomedicine XX*, vol. 9697 (International Society for Optics and Photonics, 2016), p. 96970S.

44. F. Kano, T. Yamanaka, N. Yamamoto, Y. Yoshikuni, H. Mawatari, Y. Tohmori, M. Yamamoto, and K. Yokoyama, "Reduction of linewidth enhancement factor in InGaAsP-InP modulation-doped strained multiple-quantum-well lasers," IEEE J. Quantum Electron. **29**(6), 1553–1559 (1993).

45. C.-E. Zah, R. Bhat, B. N. Pathak, F. Favire, W. Lin, M. C. Wang, N. C. Andreadakis, D. M. Hwang, M. A. Koza, T.-P. Lee, Z. Wang, D. Darby, D. Flanders, and J. J. Hsieh, "High-performance uncooled 1.3-μm $Al_xGa_yIn_{1-x-y}As/InP$ strained-layer quantum-well lasers for subscriber loop applications," IEEE J. Quantum Electron. **30**(2), 511–523 (1994).

46. L. F. Tiemeijer, P. J. A. Thijs, P. J. de Waard, J. J. M. Binsma, and T. v. Dongen, "Dependence of polarization, gain, linewidth enhancement factor, and K factor on the sign of the strain of InGaAs/InP strained-layer multiquantum well lasers," Appl. Phys. Lett. **58**(24), 2738–2740 (1991).

47. P. J. A. Thiis, L. F. Tiemeijer, J. J. M. Binsma, and T. van Dongen, "Progress in long-wavelength strained-layer InGaAs(P) quantum-well semiconductor lasers and amplifiers," IEEE J. Quantum Electron. **30**(2), 477–499 (1994).

48. H. J. S. Dorren, X. Yang, A. K. Mishra, Z. Li, H. Ju, H. de Waardt, G.-D. Khoe, T. Simoyama, H. Ishikawa, H. Kawashima, and T. Hasama, "All-optical logic based on ultrafast gain and index dynamics in a semiconductor optical amplifier," IEEE J. Sel. Top. Quantum Electron. **10**(5), 1079–1092 (2004).

49. X. Huang, Z. Zhang, C. Qin, Y. Yu, and X. Zhang, "Optimized quantum–well semiconductor optical amplifier for RZ-DPSK signal regeneration," IEEE J. Quantum Electron. **47**(6), 819–826 (2011).

50. V. S. Grigoryan, M. Shin, P. Devgan, J. Lasri, and P. Kumar, "SOA-based regenerative amplification of phase-noise-degraded DPSK signals: Dynamic analysis and demonstration," J. Lightwave Technol. **24**(1), 135–142 (2006).

51. A. J. Zilkie, J. Meier, M. Mojahedi, A. S. Helmy, P. J. Poole, P. Barrios, D. Poitras, T. J. Rotter, C. Yang, A. Stintz, K. J. Malloy, P. W. E. Smith, and J. S. Aitchison, "Time-resolved linewidth enhancement factors in quantum dot and higher-dimensional semiconductor amplifiers operating at 1.55 μm," J. Lightwave Technol. **26**(11), 1498–1509 (2008).

52. A. Mecozzi and J. Mørk, "Saturation effects in nondegenerate four-wave mixing between short optical pulses in semiconductor laser amplifiers," IEEE J. Sel. Top. Quantum Electron. **3**(5), 1190–1207 (1997).

53. A. Mecozzi and J. Mørk, "Saturation induced by picosecond pulses in semiconductor optical amplifiers," J. Opt. Soc. Am. B **14**(4), 761–770 (1997).

54. N. Storkfelt, B. Mikkelsen, D. S. Olesen, M. Yamaguchi, and K. E. Stubkjaer, "Measurement of carrier lifetime and linewidth enhancement factor for 1.5-μm ridge-waveguide laser amplifier," IEEE Photonics Technol. Lett. **3**(7), 632–634 (1991).

55. R. Clavero, F. Ramos, J. M. Martinez, and J. Marti, "All-optical flip-flop based on a single SOA-MZI," IEEE Photonics Technol. Lett. **17**(4), 843–845 (2005).

56. L. F. Tiemeijer, P. J. A. Thijs, T. van Dongen, J. J. M. Binsma, and E. J. Jansen, "Self-phase modulation coefficient of multiple-quantum-well optical amplifiers," IEEE Photonics Technol. Lett. **8**(7), 876–878 (1996).

57. A. Bilenca, S. H. Yun, G. J. Tearney, and B. E. Bouma, "Numerical study of wavelength-swept semiconductor ring lasers: the role of refractive-index nonlinearities in semiconductor optical amplifiers and implications for biomedical imaging applications," Opt. Lett. **31**(6), 760–762 (2006).

58. S. L. Girard, M. Piché, H. Chen, G. W. Schinn, W.-Y. Oh, and B. E. Bouma, "SOA fiber ring lasers: Single-versus multiple-mode oscillation," IEEE J. Sel. Top. Quantum Electron. **17**(6), 1513–1520 (2011).

59. J. Wang, A. Maitra, C. G. Poulton, W. Freude, and J. Leuthold, "Temporal dynamics of the alpha factor in semiconductor optical amplifiers," J. Lightwave Technol. **25**(3), 891–900 (2007).

60. J. Mørk and A. Mecozzi, "Theory of nondegenerate four-wave mixing between pulses in a semiconductor waveguide," IEEE J. Quantum Electron. **33**(4), 545–555 (1997).

61. Corning, "Corning SMF-28 optical fiber product information," http://www.princetel.com/datasheets/smf28e.pdf.

62. W. Wieser, G. Palte, C. M. Eigenwillig, B. R. Biedermann, T. Pfeiffer, and R. Huber, "Chromatic polarization effects of swept waveforms in FDML lasers and fiber spools," Opt. Express **20**(9), 9819–9832 (2012).

63. Corning, "Corning HI 1060 & RC HI 1060 specialty optical fibers," https://www.corning.com/media/worldwide/csm/documents/HI%201060%20Specialty%20Fiber%20PDF.pdf.

64. S. Todor, B. Biedermann, W. Wieser, R. Huber, and C. Jirauschek, "Instantaneous lineshape analysis of Fourier domain mode-locked lasers," Opt. Express **19**(9), 8802–8807 (2011).

65. S. Todor, B. Biedermann, R. Huber, and C. Jirauschek, "Balance of physical effects causing stationary operation of Fourier domain mode-locked lasers," J. Opt. Soc. Am. B **29**(4), 656–664 (2012).